Quantum Size Effect Affecting Environment Assisted Electron Capture in Quantum Confinements

Axel Molle,[1,2] Essam R. Berikaa,[3,1] Federico M. Pont,[4] and Annika Bande[1,a)]

[1)]*Institute of Methods for Material Development, Helmholtz-Zentrum Berlin für Materialien und Energie GmbH, Albert-Einstein-Str. 15, 12489 Berlin, Germany*

[2)]*Institute for Chemistry and Biochemistry, Freie Universität Berlin, Takustr. 3, 14195 Berlin*

[3)]*Department of Nanotechnology Engineering, University of Science and Technology at Zewail City, Giza, Egypt*

[4)]*Facultad de Matemática, Astronomía y Física, Universidad Nacional de Córdoba, and IFEG-CONICET, Ciudad Universitaria, Córdoba, Argentina*

(Dated: 14th March 2019)

Ultrafast inter-Coulombic electron capture (ICEC) has been established as an important energy-transfer process in open paired-quantum-dot systems which can mediate between entrapment of free-moving electrons and release of trapped ones elsewhere by long-range electron-electron interaction within nanowires. Previous studies indicated ICEC enhancement through population and secondary decay of two-center resonant bound states, the latter known as inter-Coulomb decay (ICD). This study investigates the quantum-size effect of single- and double-electron bound states in an established model of a quasi-one-dimensional nanowire with two embedded confinement sites, represented by a pair of Gaussian wells. We analyze the ICEC related electron flux density as a function of confinement size and are able to clearly identify two distinct capture channels: a direct long-ranged electron-electron impulse, and a conversion of kinetic energy to electron-electron correlation energy with consecutive ICD. The overlay of both channels make ICEC extremely likely while nanowires are a strong candidate for the next miniaturization step of integrated-circuit components.

[a)]Electronic mail: annika.bande@helmholtz-berlin.de

http://hz-b.de/theochem

I. INTRODUCTION

Size is a key factor in the electronic industry. While screens get bigger, electronic circuits become gradually smaller. Quantum effects arise which offer challenges and interesting new possibilities. Semiconductor technology has already grown and shaped electronics exponentially in the 1960s such that integrated circuits doubled the number of hosted transistors annually.[1] Known as Moore's Law, this quest for exponential reduction in electronic component size had already just reached the nanometer-scale with commercial transistors of 800 nm size in 1989[2] and has continued to fuel technological development and progress. Having reached 45 nm size in 2007,[3] current mass-produced transistors for mobile-phone processors use etched narrow fin-shaped structures approaching 7 nm thickness,[4–6] which is only three times the size of human DNA. Although the reduced size is pursued to achieve lower form factors of electronic products and higher component density on the individual integrated circuit, it offers significant technological challenges as nanometer-sized electronics leave the regime of classical physics and become governed by quantum-mechanical effects.[7] The dominating electronic components remain the same four basic elements of resistor, capacitor, (light-emitting) diode and transistor, but 100 millions of them are assembled on less than a 1 cm^2.[8]

Known as quantum size effect,[9–11] the quasi-continuous band structure of any bulk material splits up into discrete energy levels when its size is reduced sufficiently.[12,13] Similarly, regions of crystal defects, impurities, or atoms in contrast to their surrounding material can change optical and electrical properties by inducing quantum effects. Therefore, nanostructured electronic components which are essentially open quantum systems play a vital role in fostering a wealth of applications: from lasers[14] to solar cells,[15] from data storage[16] to displays,[17] from their application as sensors[18] to their potential as qbits.[19]

To further miniaturize technology to yet unachieved component density, nanowires prove to be strong candidates to reach the next research-and-development target – the so-called *5-nm node*.[20–22] We therefore investigate the confinement-size dependent capture of a free-moving electron through long-range interaction with another nearby electron confined in the vicinity as might be encountered in a device built from two quantum dots, A and B, within a nanowire.[23–26] This process has been discussed as *environment-assisted electron capture* and as *inter-Coulombic electron capture* (ICEC). It was predicted with electron dynamics for pairs of quantum dots as well as[27–29] with scattering theory for pairs of atoms and molecules.[30,31] Most recently, ab-initio R-

matrix computations demonstrated the importance of ICEC for Ne^+ in He droplets.[32] Within ICEC, an electron in an initially charged confinement B^- feels a momentum pressure through long-range Coulomb repulsion from a moving electron penetrating a neighboring confinement A. As the incident electron transfers energy to its distanced partner, it is captured into A and forces the neighboring electron to leave its respective confinement according to

$$e^-_{in} + A + B^- \longrightarrow A^- + B + e^-_{out}. \tag{1}$$

While choice of material composition and doping offers essential control over electronic device performance, it remains limited by availability, material cost and technical feasibility. Tuning the electron confinement size and thereby exploiting the quantum size effect, however, offers an alternative which is easily portable to industrial scale. This study therefore investigates how size affects efficiency and selectivity of ICEC. Electron dynamics of ICEC in quantum dots confirmed an energy-selective reaction pathway through decay of a macroscopic two-center resonance state $(AB)^*$ known by itself as *inter-Coulombic decay* (ICD), following

$$e^-_{in} + A + B^- \xrightarrow{\text{ICEC}} (A^- + B^-)^* \xrightarrow{\text{ICD}} A^- + B + e^-_{out}. \tag{2}$$

Like inter-Coulombic electron capture, ICD is mediated through long-range Coulomb interaction of electrons located on two different partner sites, may it be atoms and molecules,[33–35] or solid state confinements as quantum dots.[36–38] In the sense of a Feshbach resonance, an electron in the single-electron-excited state of one partner A^{-*} relaxes to a lower-energy state while its excess energy becomes available for ionization of the other partner B^-. Compared to the young prediction of ICEC, however, inter-Coulombic decay is already well established in various fields, among them helium droplets,[39] hollow atoms,[40] as well as biological systems,[41,42] and nanostructures as fullerenes[43] or quantum films.[44,45] Different ways to achieve ICD resonance have been studied: namely radiation,[46], α-particle,[42] and ultimately electron impact,[27–29,47] the pathway we are discussing hereafter.

The full electron dynamics of the ICEC process is going to be calculated in a charged quantum-dot-pair model of two Gaussian binding potentials.[27–29] In this comparably small system, it is possible to solve the time-dependent Schrödinger equation at a high level of numerical accuracy regarding electron-electron correlation by using the multi-configurational time-dependent Hartree (MCTDH) approach[48,49] with fermionic antisymmetrization of a discrete-variable-represented

(DVR) wavefunction as implemented in the Heidelberg implementation.[50,51] This grid-like approach bears the merit of offering access to the full electron dynamics while treating continuum states on the same footing as bound ones which is not usually achieved with many other theoretical methods.

While it was previously shown that ICD can enhance the overall ICEC probability in comparison to a direct ICEC without ICD,[27,29,52] we show in this study that the two reaction pathways are distinct in their energy signature, a broadband energy transfer echoing the incoming electron in the case of direct ICEC against energy selection through resonance criteria of ICD. As a consequence of the quantum-size effect, ICD and ICEC must depend on the size of the electronic confinements which has been investigated in the case of ICD.[53,54] Here, we intend to use the effect to study the particular interplay between ICD and ICEC, whereas a following empirical high-throughput study on ICEC in quantum dots will disentangle the particular dependence of maximal ICEC probability density on eigenenergy interrelations.[47] The primary interest in the present study is the electron flux associated with a successful inter-Coulombic electron capture in a nanowire-embedded pair of quantum dots at different confinement sizes and constant initial states. Though theoretical in nature, our investigation mimics the experimentally known and easiest access to energy-level variation of quantum dots via the well known quantum size effect.

In order to analyze the individual contributions of the inter-Coulombic electron capture channels, we describe the general evolution and kinetics of free-moving Gaussian wavepackets Sec. II A and generic decaying quantum states respectively in Sec. II B, before introducing the paired-quantum-dot model (Sec. II C) and deducing expectations towards ICEC dynamics of individual reaction channels and their distinguishability in the electron flux density (Sec. II D). Related computational details are comprised in Sec. III. To dissect the size dependence of ICEC, we start the discussion of numerical results by characterizing the traditional quantum-size effect of mono- and dielectronic eigenenergies to which there has not been any analytical solution found (Sec. IV A). Consequently, we explain an example of the evaluation of the undertaken dynamics calculation in Sec. IV B before eventually concentrating on the size dependence of the individual reaction pathways of ICEC.

II. THEORETICAL BACKGROUND

A. Free Wavepackets

A free particle moving through a medium can be described by a Gaussian wavepacket of initial average position Z, initial group velocity p_0/m^*, and initial uncertainty in position σ_z. At this point, we wish to consider one spatial dimension only which is to be denoted by z and reads

$$\langle z,t_0|\phi\rangle := \left(\frac{1}{2\pi\sigma_z^2}\right)^{\frac{1}{4}} \exp\left[-\frac{1}{4}\left(\frac{z-Z}{\sigma_z}\right)^2 + \frac{i}{\hbar}p_0(z-Z)\right]. \tag{3}$$

Although the expected position of the particle is determined up to some uncertainty at initial time t_0, it becomes less certain where it may be found as time evolves or where it would have been found at a preceding point in time. In other words, the wavepacket at t_0 has minimum uncertainty, while more generally speaking, uncertainty $\sigma_z(t)$ and average position $Z(t)$ of the wavepacket depend on time according to

$$\sigma_z^2(t) = \sigma_z^2(t_0) + \frac{i\hbar}{2m^*}(t-t_0), \tag{4}$$

$$Z(t) = Z(t_0) + \frac{p_0}{m^*}(t-t_0). \tag{5}$$

Furthermore, we can deduce the initial distribution in momentum space by the Fourier transformation of Eq. (3),

$$\langle p,t_0|\phi\rangle = \left(\frac{2\sigma_z^2}{\pi\hbar^2}\right)^{\frac{1}{4}} \exp\left[-\left(\frac{\sigma_z}{\hbar}\right)^2(p-p_0)^2 + \frac{i}{\hbar}Z(p-p_0)\right]. \tag{6}$$

By expressing the momentum in terms of energy ε as $p=-\sqrt{2m^*\varepsilon}$ for $p\le 0$ and $p=\sqrt{2m^*\varepsilon}$ for $p>0$ in the normalization integral, $1=\int_{-\infty}^{\infty}dp\,|\langle p,t_0|\phi\rangle|^2$, and then identifying the integrand as the particle's initial energy distribution by $D_\phi(\varepsilon)$, we find

$$D_\phi(\varepsilon) = \left(\frac{m^*\sigma_z^2}{\pi\hbar^2}\right)^{\frac{1}{2}} (\varepsilon)^{-\frac{1}{2}} \Bigg(\exp\left[-2\left(\frac{\sigma_z}{\hbar}\right)^2\left(\sqrt{2m^*\varepsilon}-p_0\right)^2\right] + \exp\left[-2\left(\frac{\sigma_z}{\hbar}\right)^2\left(\sqrt{2m^*\varepsilon}+p_0\right)^2\right]\Bigg). \tag{7}$$

B. Decaying States

In contrast to the state $|\phi\rangle$ of a free wavepacket, one can also consider an arbitrary metastable quantum state $|\mu\rangle$ of some sort which is to be characterized by a decay in time $t > t_0$ with decay rate $\Gamma/(2\hbar)$, energy expectation value E_μ and initial space-time-dependent amplitude $\langle z, t_0|\mu\rangle$ and reads

$$\langle z, t \geq t_0|\mu\rangle := \exp\left[-\tfrac{\Gamma}{2\hbar}(t-t_0) - \tfrac{i}{\hbar}E_\mu(t-t_0)\right]\langle z, t_0|\mu\rangle\,. \tag{8}$$

By Fourier transforming this equation, we can express the decaying state in terms of the complex Siegert energy $E_\mu - i\frac{\Gamma}{2}$ as quantum amplitude of energy E,

$$\langle z, E|\mu\rangle = \left(\frac{\hbar\Gamma}{4\pi}\right)^{\frac{1}{2}} \frac{i\left\langle z, E_\mu\middle|\mu\right\rangle}{E - \left(E_\mu - i\frac{\Gamma}{2}\right)}, \tag{9}$$

at the spatial position z with respect to the reference amplitude $\left\langle z, E_\mu\middle|\mu\right\rangle$ at energy expectation value E_μ.

It is well-known and apparent that the energy distribution $D_\mu(E)$ of such a metastable state is given by the Cauchy-distribution probability-density function

$$D_\mu(E) = \left(\frac{\hbar}{\pi\Gamma}\right)\frac{\Gamma^2}{\Gamma^2 + 4(E-E_\mu)^2} \tag{10}$$

often referred to as Lorentzian function or Breit-Wigner distribution of the resonance energy E_μ and the full-width at half-maximum Γ.[55]

C. Model System

We consider charge carriers moving along a nanowire with an embedded pair of quantum dots. This provides an example of a quasi-one-dimensional open quantum system,[21,27] where electrons can enter, pass through, and leave the medium. It allows a treatment of reduced dimensionality as carrier transport through the wire is predominantly bound to one spatial dimension.

Solid state physics generally accounts for collisions of moving charge carriers with the medium's crystal structure and other related resistant effects. This is done by assigning a material-dependent effective mass m^* to the charge carrier. By this so-called *effective mass approximation*, the carrier in the medium may then be treated analogously to a particle in free space as discussed in Sec. II A. Although the effective mass is dependent on material and other experimental conditions, the mathematical treatment becomes independent from the medium described. Consequently, it is

possible to define effective units in analogy with the free-space entities. *Atomic units* define the fundamental quanta of electron mass m_e, elementary charge e, action $\hbar$, and Coulomb force constant $(4\pi\varepsilon_0)^{-1}$ as respective units of reference, that is [1 a.u.] each. In dependence on the material, one can thus define an effective Bohr radius,[56]

$$a_B^* = \frac{4\pi\varepsilon\hbar^2}{m^* e^2} \,, \tag{11}$$

as length of reference as well as an effective energy E_H^* as reference energy analogously to the Hartree energy[56,57]

$$E_H^* = \frac{\hbar^2}{m^* a_B^{*2}}. \tag{12}$$

Accordingly, time scales in units of $\hbar/E_H^*$ and momentum in units of $\hbar/a_0$. This takes material-dependent quantities as dielectric permittivity ε and effective carrier mass m^* into account. Note that the reference scale for electric charge could similarly be adapted to the particular charge carrier considered, but shall remain the elementary charge e for the purpose of this study.

In such an effective-mass description, a local change in material or local defect in crystal structure may trap the charge beyond the statistical average. This can be described by an appropriate binding potential. The embedding of a material within another medium is thereby often modelled by a finite square box potential. Nevertheless, a different choice of potential might also account for effects like Schottky barriers,[58] energy band bending in junctions of n- and p-doped materials,[59,60] atom diffusion and wetting layer effects,[61] Fermi level unpinning[22,62], or tilted potentials inducing charge separations as found in superlattices of zinc-blendes and wurtzites.[63,64]

The nanostructure we intend to consider in this study thus consists of a virtually infinite semiconducting wire with two embedded regions of confinement at center-to-center distance $\mathscr{R}$. Assuming injected electrons as charge carriers to be described, one might talk of a p-type host material in junction with two n-type regions in the form of a pair of PNP heterojunctions. We denote the longitudinal transport direction of the wire as z and distinguish the quantum dots as the 'left' or 'right' one of respective confinement length $\mathscr{L}_L$ or $\mathscr{L}_R$ and band steps $V_{L/R}$ with respect to the surrounding wire. The smooth potential V_{QD} for this quantum-dot pair can then be modelled by the following equation which describes a pair of Gaussian wells as shown as blue line in the

bottom of Fig. 1.[36],

$$V_{QD}(z) := -D_L \exp\left[-2\left(\frac{z+\frac{\mathscr{R}}{2}}{\mathscr{L}_L}\right)^2\right] - D_R \exp\left[-2\left(\frac{z-\frac{\mathscr{R}}{2}}{\mathscr{L}_R}\right)^2\right] \tag{13}$$

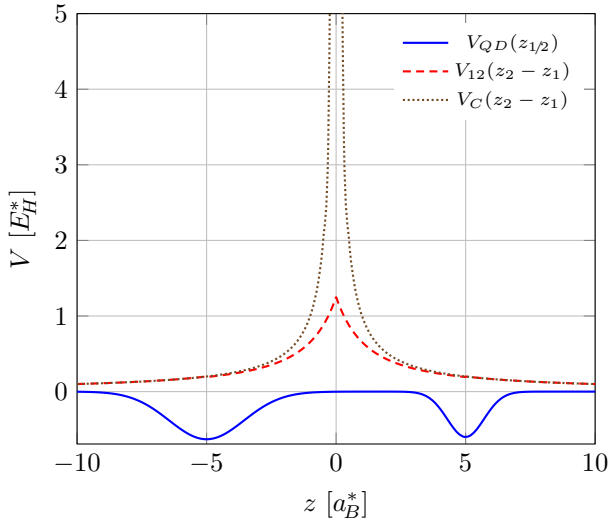

Figure 1. The binding potential V_{QD} (blue solid line) modeling the quantum dot pair as function of z is shown in conjunction with the true Coulomb potential V_C (brown dotted line) and the effective Coulomb potential V_{12} (red dashed line) as function of spatial distance $|z_2 - z_1|$ between the electrons.

We define the single-electronic Hamiltonian $\hat{h}$ of longitudinal kinetic energy and quantum-dot potential operator $V_{QD}(z)$ as

$$\hat{h} := -\frac{\hbar^2}{2m^*}\frac{\partial^2}{\partial z^2} + V_{QD}(z). \tag{14}$$

It gives rise to a set of eigenenergies $\{E_n\}_n$ and associated eigenstates $\{|n\rangle\}_n$ according to

$$\hat{h}\,|n\rangle =: E_n\,|n\rangle \quad \forall n. \tag{15}$$

For simplicity, we restrict our system to cases of a single bound state $|R\rangle$ on the right quantum dot, as well as a ground and a single excited state on the left quantum dot, $|L_0\rangle$ and $|L_1\rangle$, respectively. As localization should be distinguishable in appropriately separated quantum dots, we choose to label single-electron bound eigenstates according to their position. Unbound eigenstates are named by their free energy ε within the continuum, *i.e.*

$$\{|n\rangle\}_n =: \left\{|L_0\rangle, |R\rangle, |L_1\rangle, \{|\varepsilon\rangle\}_{\varepsilon\geq 0}\right\}. \tag{16}$$

Assuming a longitudinal setup of the charge carrying medium in the form of a wire and neglecting direct ionization out of the wire, the charge carriers are transversally bound. This means the nanowire acts as a waveguide of transversal oscillator strength $\hbar\omega_\perp$ to the particles moving through it. This has successfully been described by the harmonic potential $U_\perp$ and associated transversal ground state $|0\rangle_\perp$,[65] where a natural length l is associated to the product of oscillator strength $\hbar\omega_\perp$ and material-dependent effective mass m^* according to the equations

$$U_\perp(x,y) := \hbar\omega_\perp \left(\frac{x^2+y^2}{2l^2}\right) \tag{17}$$

$$\langle x,y|0\rangle_\perp := \left(\pi l^2\right)^{-\frac{1}{4}} \exp\left[-\frac{x^2+y^2}{2l^2}\right] \tag{18}$$

$$l := \sqrt{\frac{\hbar}{m^*\omega_\perp}}. \tag{19}$$

Generally, the Coulomb repulsion between two electrons is dependent on the distance between them with the usual $1/r$ dependence. The repulsion strength is medium dependent. The Coulomb potential $V_C(\vec{r}_1,\vec{r}_2)$ in three spatial dimensions can therefore be expressed in terms of aforementioned effective medium-incorporated units of natural scales of energy E_H^* and length a_B^* as

$$V_C(\vec{r}_1,\vec{r}_2) = E_H^* \, \frac{a_B^*}{|\vec{r}_2-\vec{r}_1|}. \tag{20}$$

We assume energies small enough to keep electrons transversally in their spatial ground-state distribution, *i.e.* $E \overset{!}{<} 3/2\hbar\omega_\perp$, while they travel longitudinally through the wire. Under this assumption, one can average over the transversal contributions to the full-dimensional Coulomb potential of interaction between a transversal electron-distribution according to Eq. (18) at longitudinal position z_1 and another one at z_2. This reduces the problem under investigation to a quasi-one-dimensional open quantum system with effective interaction potential

$$V_{12}(z_1,z_2) = E_H^* \, \frac{a_B^*}{l} \sqrt{\tfrac{\pi}{2}} \, w\left(i\frac{|z_2-z_1|}{\sqrt{2}l}\right) \tag{21}$$

$$\text{with } w(iz) := \left(1-\text{erf}[z]\right) \, \exp\left[z^2\right]. \tag{22}$$

and has been employed successfully.[27,29,38] Note here, that $w(iz)$ is the Faddeeva function,[66] and the effective potential V_{12} thus exhibits a shape related to the Voigt profile (dashed line in Fig. 1)[66] compared to the diverging profile of the true Coulomb interaction $V_C(\vec{r}_1,\vec{r}_2)$ displayed for $x_{1/2} = y_{1/2} = 0$ (Fig. 1, dotted line).

Due to the fermionic nature of the two electrons investigated here, their total wavefunction has to obey Pauli's exclusion principle. The wavefunction describing an electron in an arbitrary state $|\alpha\rangle$ and another in an arbitrary state $|\beta\rangle$ shall hence be given by their antisymmetric outer product and denoted by $|\alpha\beta\rangle$.

$$|\alpha\beta\rangle := \tfrac{1}{\sqrt{2}}\big(|\alpha\rangle\otimes|\beta\rangle - |\beta\rangle\otimes|\alpha\rangle\big) \tag{23}$$

Accordingly, a projection of the overall wavefunction onto the two-electron state $|\alpha\beta\rangle$ is defined by the outer product of state with itself and is being denoted

$$\hat{\mathbb{P}}_{\alpha\beta} := |\alpha\beta\rangle\langle\alpha\beta| \tag{24}$$

Furthermore, we wish to consider a projection $\hat{\mathbb{P}}_\alpha$ of the two-electron wavefunction on an arbitrary single-electron state $|\alpha\rangle$, which describes the wavefunction of one electron coinciding with another one occupying state $|\alpha\rangle$. Such a projector is mathematically described by the symmetric outer product of state $|\alpha\rangle$ with the identity operator $\mathbb{1}$ as

$$\hat{\mathbb{P}}_\alpha = \tfrac{1}{2}\big(|\alpha\rangle\langle\alpha|\otimes\mathbb{1} + \mathbb{1}\otimes|\alpha\rangle\langle\alpha|\big) \tag{25}$$

We wish to numerically undertake an ICEC experiment. For that purpose, we charge the right quantum confinement and send a free electron towards the paired quantum confinement from the left. That means we prepare an electron in bound state $|R\rangle$, and another in free state $|\phi\rangle$ according to Eq. (3) at a large distance from the quantum-confinement region. We then antisymmetrize according to Eq. (23) to reach the total state $|\Psi\rangle$. In general, $|\Psi\rangle$ is not separable into single-electron components due to electron-electron interaction. At an infinite distance, however, the electrons cannot interact and are effectively independent from each other. This implies the two-electron wavefunction $\langle z_1, z_2|\Psi\rangle$ can be well approximated by antisymmetrically combined single-electronic components within the large-distance limit as

$$\langle t = t_0|\Psi\rangle \quad := \quad |\phi R\rangle \quad = \quad \tfrac{1}{\sqrt{2}}\big(|\phi\rangle \otimes |R\rangle - |R\rangle \otimes |\phi\rangle\big). \tag{26}$$

As we wish to consider two-electron states from here on, we use indices '1' or '2' to indicate single-electronic quantities where appropriate. The Hamilton operator $\hat{h}_1$, for example, shall refer to the operator sum of quantum-confinement potential V_{QD} and kinetic energy operator as introduced in Eqs. (13) and (14) which act on the electron labelled by '1'. Further the electronic interaction potential V_{12} is contained. We thereby arrive at the system's Hamiltonian operator

$$\hat{H} = \hat{h}_1 + \hat{h}_2 + V_{12}. \tag{27}$$

D. ICEC Dynamics

Analyzing the evolving state $|\Psi\rangle$ at large times, we can assure that inter-Coulomb electron capture has taken place if we observe an electronic current at a large distance from the confinement region coinciding with some occupation of the left-bound single-electron states $|L_0\rangle$ and $|L_1\rangle$. We therefore define the flux operator $\hat{F}$ such that its expectation value $F(t)$ as function of time describes the electron flux at longitudinal position z_F. Respectively, $F(E)$ describes the energy distribution of the electron flux passing through longitudinal position z_F. Electron flux through z_F that coincides with the simultaneous occupation of the single-electron state $|L_0\rangle$ is consequently described by applying the operator $\hat{\mathbb{P}}_{L_0}^\dagger \hat{F} \hat{\mathbb{P}}_{L_0}$. Its time- or energy-dependent expectation value is going to be denoted by $F_{L_0}(t)$ and $F_{L_0}(E)$, respectively, hence as

$$F_{L_0}(t) := \left| \left\langle \Psi \middle| \hat{\mathbb{P}}_{L_0}^\dagger \middle| t \right\rangle \left\langle t \middle| \hat{F} \middle| t \right\rangle \left\langle t \middle| \hat{\mathbb{P}}_{L_0} \middle| \Psi \right\rangle \right|, \tag{28}$$

$$F_{L_0}(E) := \left| \left\langle \Psi \middle| \hat{\mathbb{P}}_{L_0}^\dagger \middle| E \right\rangle \left\langle E \middle| \hat{F} \middle| E \right\rangle \left\langle E \middle| \hat{\mathbb{P}}_{L_0} \middle| \Psi \right\rangle \right|. \tag{29}$$

Because the initial wavefunction is not equally distributed over the entire energy range, the measured flux will depend on the energy distribution

$$D_{\Psi_0}(E) := \left| \langle \Psi_0 | E \rangle \langle E | \Psi_0 \rangle \right|. \tag{30}$$

The probability density for a successful inter-quantum-dot Coulombic electron capture into $|L_0\rangle$ within the infinitesimal range of total energy from E to $E + dE$ is hence given by the fraction of measured electron flux of that energy by available density distribution,

$$P_{L_0}(E) := \frac{F_{L_0}(E)}{D_{\Psi_0}(E)}, \quad \text{if } D_{\Psi_0}(E) > 0. \tag{31}$$

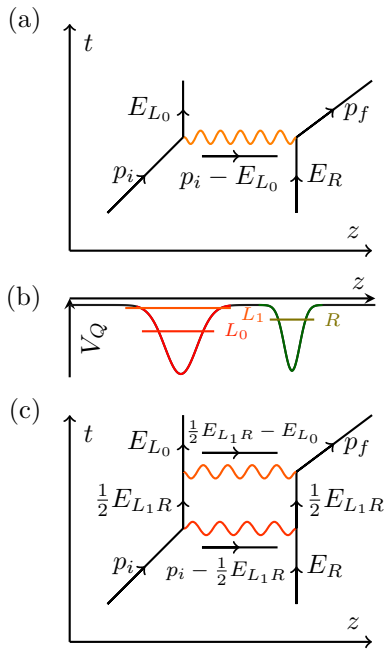

Figure 2. (b) The binding potential V_{QD} modeling the quantum dot pair as function of z is shown and the energy levels of the states L_0, R, L_1 are indicated. (a) shows the diagram of direct ICEC in alignment with the binding potentials of (b). Arrows indicate the electron evolution in space and time with momentum $p_{i/f}$ or only in time when being in one state of energy $E_{L0/R}$. The wiggled lines represent the transferred energy. (c) The representation of direct ICEC is supplemented with the representation of the resonant ICEC.

Any evolution has to conserve the total energy E_T of the system. So energy transferred through a capture into $|L_0\rangle$ has to equal the energy difference between right-bound $|R\rangle$ and left-bound $|L_0\rangle$

$$\frac{{p_i}^2}{2m^*} + E_R = E_T \tag{32}$$

$$E_T = E_{L_0} + \frac{{p_f}^2}{2m^*}. \tag{33}$$

This is diagrammatically presented in Fig. 2 (a). Despite the electronic correlations throughout the process, this means that energy transfer is solely dependent on single-electron quantities. Under the assumption that a metastably bound two-electron excited state can be occupied which might bear at least conceptual similarities with a state of simultaneously occupied $|L_1\rangle$ and $|R\rangle$ in consequential perturbation by respective repulsion, we call this state $|L_1R\rangle$. If such a state is to be populated by the evolving state $|\Psi\rangle$ at some point in time $t \geq t_0$, energy conservation must be ensured equally. As such, only those fractions of incoming wavepacket can contribute which are

appropriately energetically situated close to the energy difference (*cf.* see Eq. (10)) between E_{L_1R} and E_R, as depicted in diagram (c) of Fig. 2, *i.e.*

$$\frac{{p_i}^2}{2m^*} + E_R = E_{L_1R} \tag{34}$$

$$E_{L_1R} = E_{L_0} + \frac{{p_f}^2}{2m^*} \tag{35}$$

Similarly, the kinetic energy release coinciding with a residual occupation in L_0 depends on the energy difference between E_{L_1R} and E_{L_0} as this intermediate state decays by tunneling out of the Coulomb-induced confinement barriers. Nevertheless, despite its particular dynamics via $|L_1R\rangle$, the overall excess kinetic energy remains independent of E_{L_1R} and depends solely on the single-electronic quantities E_{L_0} and E_R.

If we assume ICEC to occur as an elastic scattering in the form of a direct energy transfer or impulse between the two electrons, we would expect an electron flux energetically similar to the initial energy distribution $D_\phi(\varepsilon)$. The energy distribution $D_{\Psi_0}(E_T)$ of the initial state $|\Psi_0\rangle$ is trivially separable into its electronic components, as the incoming wavepacket $|\phi\rangle$ and the right-bound electron $|R\rangle$ are at very large distance from each other and correlative interaction is negligible,

$$D_{\Psi_0}(E_T) = D_\phi(\varepsilon) \times \delta(E_R - (E_T - \varepsilon)), \text{ for } E_T =: \varepsilon + E_R. \tag{36}$$

Due to equations (7), (15), and (16), we expect the energy distribution $D_{\Psi_0}(E_T)$ to be a simple superposition of continuous contributions of free energy ε and discrete eigenenergy E_R,

$$\begin{aligned} F_{L_0}^{\phi}(\varepsilon) &\propto \left|\langle E_T - E_R|\phi\rangle\right|^2 \\ &\propto \frac{p_0}{\sqrt{2m^*\varepsilon}} \frac{\exp\left[-2\frac{\sigma_z^2 p_0^2}{\hbar^2}\left(\frac{\sqrt{2m^*\varepsilon}}{p_0} - 1\right)^2\right]}{1+\exp\left[-8\frac{\sigma_z^2 p_0^2}{\hbar^2}\right]} \\ &\quad + \frac{p_0}{\sqrt{2m^*\varepsilon}} \frac{\exp\left[-2\frac{\sigma_z^2 p_0^2}{\hbar^2}\left(\frac{\sqrt{2m^*\varepsilon}}{p_0} + 1\right)^2\right]}{1+\exp\left[-8\frac{\sigma_z^2 p_0^2}{\hbar^2}\right]}, \end{aligned} \tag{37}$$

where the second term is expected to have a very small contribution near $\varepsilon = p_0^2/2m^*$.

On the other hand, assuming that the kinetic energy of the initially free wavepacket is transferred into correlation energy between the electrons, electron capture might occur initially without environmental ionization. The interaction between both bound electrons then allows a secondary energy transfer resulting in electron tunneling out of the confinement. As this two-electron bound

state thus decays, we expect the electronic flux to reflect this decay according to Eqs. (10) and $F_{L_0}^{L_1R}(E_T)$ should show a Breit-Wigner shape, *i.e.*

$$F_{L_0}^{L_1R}(E_T) \propto \left|\langle E_T|L_1R\rangle\right|^2 \propto \frac{\Gamma^2}{4(E_T-E_{L_1R})^2+\Gamma^2}. \tag{38}$$

Consequently, electron capture through both processes, direct impact of $|\phi\rangle$ on $|R\rangle$ and inter-quantum-dot Coulombic decay of $|L_1R\rangle$, has to show the usual quantum mechanical superposition of amplitudes resulting in some interference term according to a complex phase difference φ between both. We can therefore evaluate the probability density for the infinitesimal energy range $E_T \ldots (E_T + dE_T)$ for a successful inter-quantum-dot Coulombic electron capture according to Eq. (31). Numerically, this definition proves to be limited to a certain confidence interval in energy for which the initial energy distribution $D_\phi(E_T - E_R)$ is confidently non-vanishing in order to avoid division by 0. Note that the flux $F_{L_0}(E_T)$ can also be evaluated for regions outside the energy confidence interval as

$$F_{L_0}(E_T) \propto \left|K_\phi\ \langle E_T - E_R|\phi\rangle + K_{L_1R}\ \langle E_T|L_1R\rangle\right|^2, \tag{39}$$

$$P_{L_0}(E_T) \propto \frac{\left|K_\phi\ \langle E_T - E_R|\phi\rangle + K_{L_1R}\ \langle E_T|L_1R\rangle\right|^2}{D_\phi(E_T-E_R)}, \quad \text{if } D_\phi(E_T-E_R) > 0. \tag{40}$$

III. COMPUTATIONAL DETAILS

We numerically apply the multi-configurational time-dependent Hartree (MCTDH) approach with antisymmetrization to describe and propagate the quantum-mechanical two-electron wave-function of form[48,49]

$$\Psi(z_1,z_2,t) := \sum_{j_1,j_2=1}^{N_1,N_2} A_{j_1j_2}(t)\chi_{j_1}(z_1,t)\chi_{j_2}(z_2,t). \tag{41}$$

It contains the Hartree product of time-dependent single-particle functions (SPFs)

$$\chi_j(z,t) := \sum_{m=1}^{M} c_j^{(m)}(t) b_m(z). \tag{42}$$

Their primitive basis, $\{b_m(z)\}_{m=1}^M$, is given within a Sine (Chebyshev) discrete variable representation (DVR) of 431 grid points each between $z = -270.0\,a_B^*$ and $+270.0\,a_B^*$ for both electronic z

coordinates (see Tab. I). The configuration space, $N_1 \times N_2$, taken into account is of size 14×14 for the initial preparation of state and then reduced to configurations of triplet states by enforcing the identical nature of both electrons and antisymmetric coefficients through

$$A_{j_1 j_2}(t) \stackrel{!}{=} -A_{j_2 j_1}(t) \; \forall t. \tag{43}$$

While initially separable as both electrons are at large distance from each other, electron correlation grows with time when the electrons approach each other. Numerically this means that the wavefunction is initially well-described by a single configuration, while with increasing time, the configuration space becomes more widely populated.

As described in the theory section, Sec. II Eq. (26), the initial wavefunction is prepared by an antisymmetric superposition of a free electron wavepacket of Gaussian form and the bound single-electron eigenfunction of the quantum dot localized at the right $|R\rangle$. The Gaussian wavepacket is initially centered at $Z = -125\,a_B^*$ with group momentum $p_0 = 0.335\,\hbar/a_B^*$ and root-mean-square (rms) width σ_z of $10.0\,a_B^*$, where all units are effective atomic units and scaled with respect to an effective electron mass of unity. We summarize the employed parameters concisely for better legibility and reference in Tab. I.

The transversal oscillator strength of the nanowire is set to $\hbar\omega_\perp = 1.0\,E_H^*$. This implies a natural length scale equal to the characteristic length scale, a_B^*, of the chosen material according to Eq. (18). The right quantum dot and inter-dot distance are kept constant throughout this study which ensures a constant initial wavefunction. With a rms width of $1/\sqrt{2}\,a_B^*$, such that $b_R = 1.0\,a_B^{*-2}$, the right quantum dot is set to an effective energy minimum of $D_R = 0.60\,E_H^*$ and at a distance from quantum-dot center to center of $R = 10.0\,a_B^*$ (compare Ref. 29). The left quantum dot is fixed with an effective binding energy of $D_L = 0.71\,E_H^*$ and is being varied in size between a length (i.e. double rms width) of $\mathscr{L}_L = 3.6\,a_B^*$ and $0.7\,a_B^*$.

In order to prevent unphysical reflections of the electron wavefunction at the edges of the grid and to avoid consequent self-interference, complex absorbing potentials $\hat{W}$ with

$$-i\hat{W} := -i\eta \left(\frac{|z - z_{cap}|}{a_B^*}\right)^n \times \Theta\left[-k\left(\frac{z - z_{cap}}{a_B^*}\right)\right] \tag{44}$$

of quadratic order, $n = 2$, have been placed with the Heaviside function $\Theta(z)$ at $z_{cap} = \pm 168.75\,a_B^*$ in order to collect outgoing fractions of the wavepacket.[67–70] The parameter η is computed to maximize the absorption and minimize reflection from the edges. See Tab. I for details.

Table I. Collection of computational parameters of the system.

Incident electron parameters, see Eqs. (3), (19)			
$p_0 = 0.335\,\hbar/a_B^*$	$Z = -125\,a_B^*$	$\sigma_z = 10.0\,a_B^*$	$l = 1.0\,a_B^*$
Quantum-dot-pair parameters, see Eq. (13)			
$\mathscr{L}_L \in \{0.7\,a_B^*,\ \ldots,\ 3.6\,a_B^*\}$		$D_L = 0.71\,E_H^*$	
$\mathscr{L}_R = 0.707\,a_B^*$		$D_R = 0.60\,E_H^*$	
$\mathscr{R} = 10.0\,a_B^*$			
DVR type	grid points	z range	
Sine	431	$-270.0\,a_B^*$	$+270.0\,a_B^*$
SPF configurations		14×14, *id*	
CAP z_{cap}	η	n	k
$-168.75\,a_B^*$	$5.79 \cdot 10^{-6}\,E_H^*$	2	-1
$+168.75\,a_B^*$	$5.79 \cdot 10^{-6}\,E_H^*$	2	$+1$

IV. RESULTS

Before we analyze the dynamics of ICEC, we need to characterize the variation of static quantities with the confinement size. We thus wish to study the observed changes in single-electron eigenenergies E_{L_0} and E_{L_1} first, before discussing electron-electron correlation energies and distances in the two-electron states $|L_0R\rangle$ and $|L_1R\rangle$. With that at hand, we plan to explain an example of the undertaken flux analysis on the full electron dynamics and eventually show six different cases of ICEC flux profiles indicating the contributions via direct ICEC and secondary ICD.

A. Quantum-Size Effect of Stationary Quantities

In the investigated range of sizes between $\mathscr{L}_L = 0.7\,a_B^*$ and $3.6\,a_B^*$, the numerical results of the dependence of single-electron eigenenergies E_{L_0}, E_R and E_{L_1} are depicted in Fig. 3 (a) as lines in violet with diamonds, in blue with triangles, and in turquoise with pentagons. As the right quantum dot has not been changed throughout, E_R is constant over the whole range of $\mathscr{L}_L$, whereas both left quantum dot energies decrease monotonically with increasing $\mathscr{L}_L$. Note that the quantum dot contains a second L_1 level only for $\mathscr{L}_L \geq 0.9 a_B^*$ and that the drop in E_{L_1} is slow in the beginning

until it starts to follow that of E_{L_0} from approximately $\mathscr{L}_L \geq 2.2a_B^*$ onward.

We find that the observed trend is empirically well-described by a second-order polynomial of powers of square-roots of length, $E_{L_k}(\mathscr{L}_L) = \mathscr{P}^{(k)}(\sqrt{\mathscr{L}_L}) = a_0^{(k)} + a_1^{(k)}\sqrt{\mathscr{L}_L} + a_2^{(k)}\mathscr{L}_L$, for both left-located eigenenergies E_{L_k} available in the regime. In fact, due to the limited range of bound L_1 in our sampling, the linear offset energy, $a_0^{(1)}$, can be set to zero and the two parameters, $a_1^{(1)}$ and $a_2^{(1)}$, suffice to describe the size effect efficiently for the 11 data points of negative E_{L_1} with a relative uncertainty of less than 1.3% in either parameter and a root-mean-square residual of $1.5 \times 10^{-3} E_H^*$. We find thus $a_1^{(1)} = 0.289(4)E_H^*/\sqrt{a_B^*}$ and $a_2^{(1)} = -0.199(3)E_H^*/a_B^{*2}$. Respectively, the 21 data points for L_0 are empirically described by parameters $a_0^{(0)} = 0.472(4)E_H^*$, $a_1^{(0)} = -0.864(5)E_H^*/\sqrt{a_B^*}$ and $a_2^{(0)} = 0.184(2)E_H^*/a_B^{*2}$ with respective relative uncertainties below 1.0% rms residual of $0.7 \times 10^{-3} E_H^*$.

While known analytical solutions to eigenvalue problems of quantum mechanical potentials – like the quantum-harmonic oscillator, the infinite or finite square well, the Pöschl-Teller or Morse potential – suggest an expansion in powers of n and $\mathscr{L}_L^{-1}$ rather than square roots of length, such a second order Polynomial only yields a rms residual of $3.2 \times 10^{-3} E_H^*$ for the quantum size effect in L_0 and deviates from the numerical results in its behavior which is particularly perceptible at lower sizes around $1.0\,a_B^*$. A third order term is able to correct this behavior and to reduce the rms residual to $0.2 \times 10^{-3} E_H^*$ for L_0. It also allows a smoother transition of the L_1 eigenenergy towards zero. Nevertheless, this suggested otherwise little advantage over the simpler description in orders of $\sqrt{\mathscr{L}}$ for the investigated size range.

In Fig. 3 (a) we also depict the constant total $\langle E_T \rangle$ (green line with hollow squares, *cf.* Eqs. (32) and (26)) as well as the energy difference $\langle E_T \rangle - E_{L_0}$ (red line with $\oplus$ symbols) and the unchanged initial momentum p_0 (ocre triple line with $\otimes$ symbols). From all the curves together we can make out distinct crossing points. Just above the selected $\mathscr{L}_L$ region the crossing of E_{L_1} and E_R as well as $\langle E_T \rangle$ is expected. Another point that was highlighted in earlier investigations on ICEC as function of D_L, is the crossing of $\langle E_T \rangle$ with $E_{L_0} - E_R$ and $E_{L_1 R}$ all together, where the highest ICEC probability due to favorable energy conditions for resonance ICEC was found.[29] Here we only see crossing points near $\mathscr{L}_L = 1.125\,a_B^*$ where the left confinement has only one bound state. E_{L_0} crosses with E_R and $\langle E_T \rangle - E_{L_0}$ with p_0. The specialty of the system at this length can be revealed when considering the two-electron quantities as well.

In Fig. 3 (b) we plot the expectation values of the interaction strength, the effective Coulomb energy V_{12}, as a function of $\mathscr{L}_L$. It was calculated according to $E_{L_k R} - E_{L_k} - E_R$ for the two-

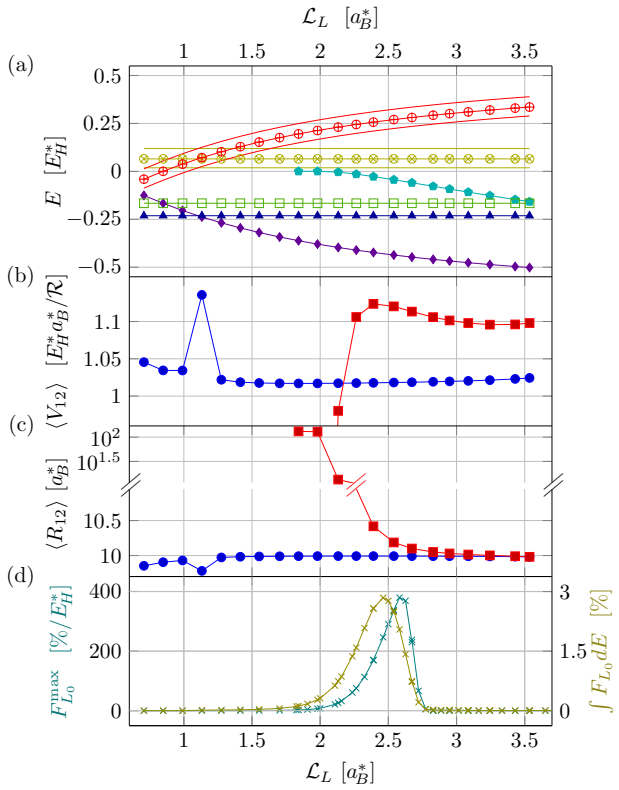

Figure 3. The key figures of the system of two quantum dots in a nanowire are displayed as function of $\mathscr{L}_L$ in a_B^*. (a) Energy and momentum contributions are shown. For the single-electron energies, lines with violet diamonds represent E_{L_0}, with blue triangles E_R, and with turquoise pentagons (setting on for $\mathscr{L}_L \geq 0.9 a_B^*$) E_{L_1}. The constant transferred energy $\langle E_T \rangle$ is shown as green line with hollow squares. The range of available final energies $\langle E_T \rangle - E_{L_0}$ is indicated by a red line with $\oplus$ symbols, adjacent red lines mark three standard deviations $\sigma_\varepsilon^\pm = \hbar/(2m^*\sigma_z)(p_0 \pm \hbar/(4\sigma_z))$. The unchanged initial kinetic energy $p_0^2/(2m^*) \pm 3\sigma_\varepsilon^\pm$ with three standard deviations is displayed by ochre triple line with $\otimes$ symbols. (b) Coulomb interaction $\langle V_{12}\rangle$ for $|L_0R\rangle$ (blue dots) and $|L_1R\rangle$ (red squares) obtained from $E_{L_kR} - E_{L_k} - E_R$ and scaled by $1/\mathscr{R}$. (c) Effective distances $\langle R_{12}\rangle = \langle |z_2 - z_1| \rangle$ for states as in (b). Note the scale breaking. (d) Maximal flux $F_{L_0}^{max}$ (turquoise with peak at $\mathscr{L}_L \approx 2.6 a_B^*$) and integrated flux $\int F_{L_0} dE$ (green line with peak at $\mathscr{L}_L \approx 2.45 a_B^*$ with distinct scales of the ordinate.

electron ground state $|L_0R\rangle$ (blue dots) and the resonance $|L_1R\rangle$ (red squares). In Fig. 3 (c), lines with the same color code are used to depict the respective electron-electron distance $|\langle z_2 - z_1 \rangle|$ from $|L_0R\rangle$ and $|L_1R\rangle$ of (b). These quantities have been determined to quantify their difference from the estimate of $V_{12} \approx 1/\mathscr{R}$. For the lowest two-electron bound state of the system, $|L_0R\rangle$, the average expectation of ground state interaction strength in our sampling lies 2.75% above the

approximation of $1/\mathscr{R} = 0.10\,E_H^*$. Peaking with an expectation value of $\langle V_{L_0R}\rangle = 0.1136\,E_H^*$ at a quantum-dot length of $1.13\,a_B^*$ around where the single-electronic eigenenergies E_{L_0} and E_R cross, the limited resolution suggests a lambda transitional shape. For a narrow left quantum dot below $1.0\,a_B^*$, the expectation value appears to significantly increase as the bound electron delocalizes due to the close threshold energy. For lengths above $1.5\,a_B^*$, electronic interaction increases slowly as separation between the quantum dots reduces together while the left quantum dot grows equally to the left. Within the investigated range, the minimal interaction strength in the two-electron ground state is found with $0.1017\,E_H^*$ at longitudinal quantum-dot size of $1.84\,a_B^*$.

In comparison, the resonant energy level $|L_1R\rangle$ shows a mean expectation value of interaction strength $\langle V_{12}\rangle$ 10.58% above the approximated $1/\mathscr{R} = 0.10\,E_H^*$. It deviates from the approximate by the order of the system's kinetic energy. This estimate proves therefore only a crude approximation. From its minimal electronic interaction of $0.1096\,E_H^*$ at left quantum dot size of $3.24\,a_B^*$, electronic repulsion increases with E_{L_1} as the quantum dot narrows. It climaxes with $0.1124\,E_H^*$ at a size of $2.39\,a_B^*$ where increase in eigenenergy is balanced by the increasingly available localization range as the quantum dot potential spreads with length $\mathscr{L}_L$. Electronic interaction therefore drops steeply around the zero transition of $|L_1\rangle$ as the wavefunction extends toward $-\infty$ when the eigenvalue is being pushed out of the binding potential. Similarly to electronic repulsion in the ground state $|L_0R\rangle$, we observe a slow repulsive rise for higher sizes as the quantum-dot barrier reduces until the quantum-dot pair amalgamates.

While the electrons are bound by the respective quantum-dot potentials, we expect electronic repulsion to polarize the individual quantum dot such that the average electron densities are slightly shifted and one could naïvely assume the repulsive force to hold the electrons outwards from their original non-interacting equilibrium position, $|\langle z_2 - z_1\rangle| \gtrsim \mathscr{R}$. Surprisingly, we find the expectation value of inter-electronic distance (see Fig. 3 (c)) in the ground state $|L_0R\rangle$ continuously slightly smaller than the distance between the respective quantum-dot centers with a mean electron-electron distance of $9.995(12)\,a_B^*$ with the uncertainty given in parentheses. We particularly observe a general reduction of electronic distance at $\mathscr{L}_L < 2\,a_B^*$ and an intermediate drop at $\mathscr{L}_L = 1.13(15)\,a_B^*$ as the left and right-localized eigenenergies cross and direct tunneling opens up the available space. This behavior partially counteracts the trend in $\langle V_{12}\rangle$ of Fig. 3 (b).

For the two-electron excited state $|L_1R\rangle$, we find a strong quantum size dependence of the expectation value of inter-electronic distance. We measure an expectation value $\langle \mathscr{R}_{12}\rangle = |\langle z_2 - z_1\rangle_{L_1R}| = 9.982(4)\,a_B^*$ at left quantum-dot size $\mathscr{L}_L = 3.50\,a_B^*$ and $\langle \mathscr{R}_{12}\rangle = 10.25(7)\,a_B^*$ at $\mathscr{L}_L = 2.50\,a_B^*$. Nar-

rowing the left quantum dot further raises the inter-electronic distance with the eigenenergy E_{L_1}. This opens up a wider range between the potential reflection points as the potential approaches the continuum, such that $\langle \mathscr{R}_{12} \rangle = (19 \pm 6)\, a_B^*$ at $\mathscr{L}_L = 2.125\, a_B^*$ before the localization of $|L_1\rangle$ breaks down. The overall trend is inverse to the behavior of $\langle V_{12} \rangle$. Only in the range $2.39\, a_B^* < \mathscr{L}_L < 3.20\, a_B^*$, interestingly, the system simultaneously allows an increased expectation value of Coulomb interaction $\langle V_{12} \rangle_{L_1 R} > \frac{1}{\mathscr{R}}$ despite an expanded expectation value in electron-electron distance $\langle \mathscr{R}_{12} \rangle > \mathscr{R}$ for most of the investigated quantum-dot-size range before the vanishing of $|L_1\rangle$ into the continuum.

B. ICEC Dynamics

Having investigated single-electron eigenenergies of the system and electron-electron correlated two-electron intermediate states as precursors to analyze the full ICEC dynamics, we would like to discuss with $\mathscr{L}_L = 2.83\, a_B^*$ an exemplary case of the flux analysis at this point. Investigating the time-dependent spatial probability-density $|\Psi(t)|^2$ based on Eqs. (26) and (41) as depicted in the lower panel of Fig. 4, we find that for the first times up to $210\hbar/E_H^*$ the incoming electron approaches the right-bound one coming from the negative z direction. During this time we observe a broadening of the incoming wavepacket in time due to its dispersion. From impact, we observe a spray of electron probability density leaving in positive z direction with increased velocity in comparison to the incoming one notable at the steeper slope $\Delta z/\Delta t$. At the same time, we observe interference ridges in negative z direction, as fractions of the incoming wavefront are being reflected back to the left and interfere with fractions still traveling towards the double confinement. Note that immediately from the impact, we also observe a double line at the position of the left quantum dot indicating a binding to the left-excited state $|L_1\rangle$. The first wave of right-bound electron release terminates around $550\hbar/E_H^*$. We further observe a revival of a second wave of right-bound electron release around $650\hbar/E_H^*$ to $1050\hbar/E_H^*$. At the same time, we note a loss of resolution in the left-bound double peak which indicates consecutively with the simultaneous right-bound ionization an active ICD process. Both of those electron probability waves were measurable as flux of time $F_{L_0}(t)$ (Eq. (28) and upper panel of Fig. 4) in coincidence with an occupied left-bound ground state $|L_0\rangle$ with maximum at time $550\hbar/E_H^*$ and therefore confirm to be the result of an inter-quantum-dot Coulombic electron capture.

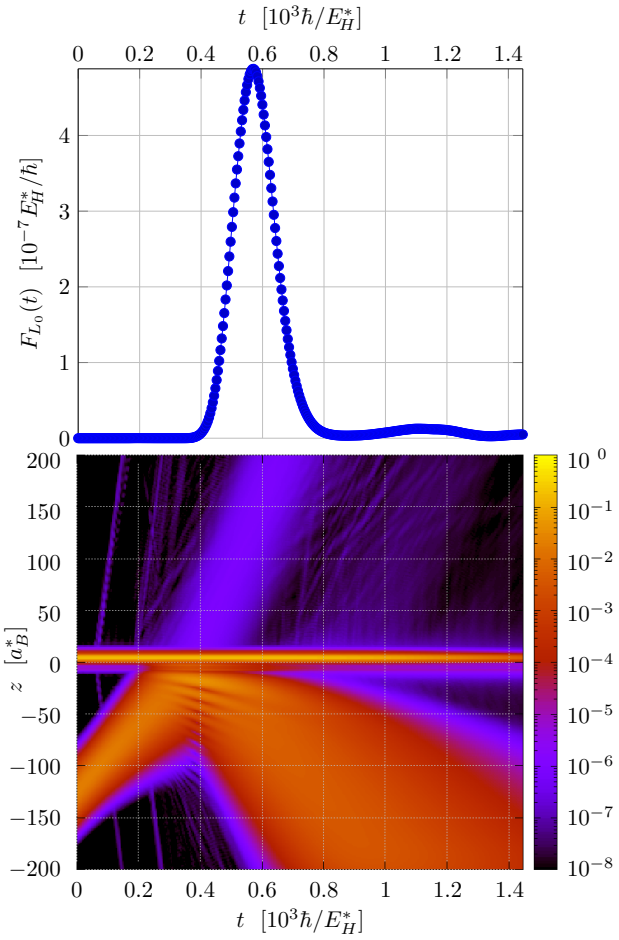

Figure 4. Lower panel: evolution of the spatial probability density $|\Psi(t)|^2$ with time (see Eqs. (26) and (41). Upper panel: time-dependent electron flux $F_{L_0}(t)$ through wire at longitudinal position z_F in coincidence with the capture of electron density in the left quantum dot's ground state $|L_0\rangle$ for the case of $\mathscr{L}_L = 2.83 a_B^*$.

In order to consequently investigate the confinement-size dependent ICEC through the measured flux, we Fourier transform the measured electron release in time to arrive at an energy dependent flux profile $F_{L_0}(E)$ (Eq. (39), red solid lines and left axis labels in panels of Fig. 5, and solid lines in Fig. 6). Already for the discussed geometry with $\mathscr{L}_L = 2.83\, a_B^*$ in the bottom left panel of Fig. 5, we observe as expected a superposition in the electron flux profile of a Breit-Wigner resonance shape (left peak) and an energy distribution related to a normally distributed momentum (right peak). The flux profile fits expectations according to Eq. (39) (see Fig. 5 gray solid line beneath red one, left axis labels). As discussed, we can attribute the Breit-Wigner, or Lorentzian contribution according to Eq. (10) to a decay process of an intermediate state which energetically bears the energy signature of a double-electronic occupation of $|L_1 R\rangle$ with electron-

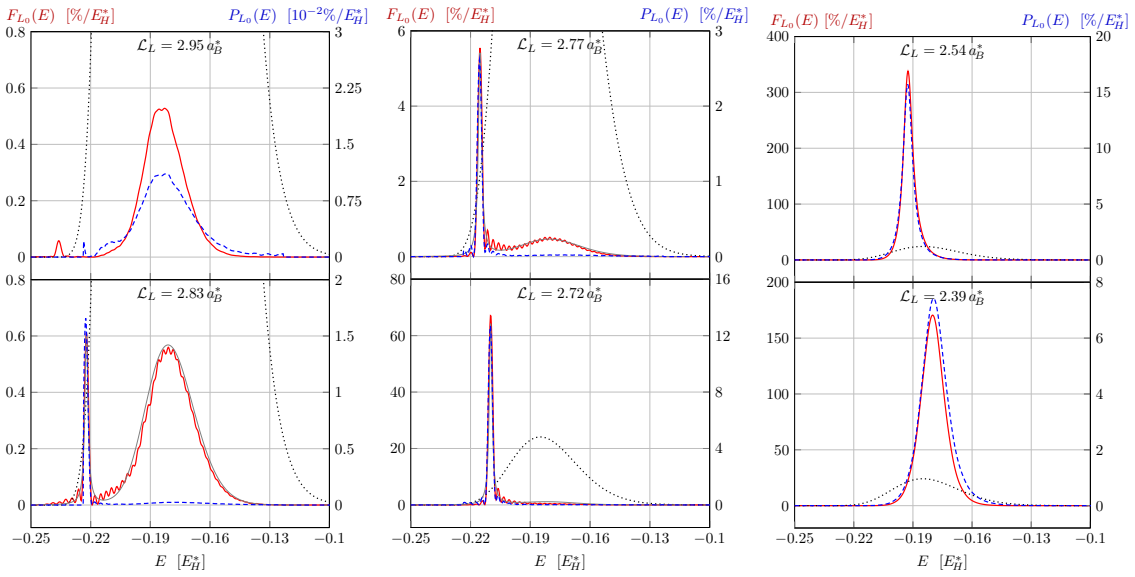

Figure 5. All panels show the electron flux density $F(E)$ of Eq. (29) as red solid line, together with the fitting result to it (Eq. (39)) as adjacent grey solid line. Further the initial wave packet energy distribution (see Eq. (7), yellow dotted line) and the ICEC probability density $P(E)$ (see Eq. (40), blue dashed line) are displayed. Panels differ by underlying $\mathscr{L}_L$ with values $2.95\,a_B^*$ (top left), $2.83\,a_B^*$ (bottom left), $2.83\,a_B^*$ (top middle), $2.72\,a_B^*$ (bottom middle), $2.54\,a_B^*$ (top right), and $2.39\,a_B^*$ (bottom right).

electron correlation energy. We further find that the other contribution coincides with the shape of the initial free wavepacket according to Eq. (7).

While the panels of Fig. 5 show flux profiles for particular confinement sizes, Fig. 6 compares their intensities and maximal positions directly. As we pass through the geometries along decreasing $\mathscr{L}_L$ the resonance energy for the ICD decay varies with the quantum size effect, while the wavepacket energy distribution is a constant throughout our study (thin dotted lines in Fig. 5). As a result, the $F(E)$ maxima of ICD resonances lie at different energies than the wavepacket maximum but are modulated in maximal intensity by the underlying shape of the wavepacket.

As the flux profile exhibits the usual quantum mechanical superposition according to Eq. (39), we note the variation in composed shape of the flux profile as the ICD resonance passes through the contribution of direct impulse. As both energies get closer, the process signatures become harder to distinguish as can be seen from the last three panels of Fig. 5. As they overlap, the flux profile appears to be of Breit-Wigner shape at first glance in accord with former predictions,[29] but remains a superposition of both processes. Nevertheless, it is still numerically obvious that a decay-describing Lorentzian function can only partially account for the entire shape. We note

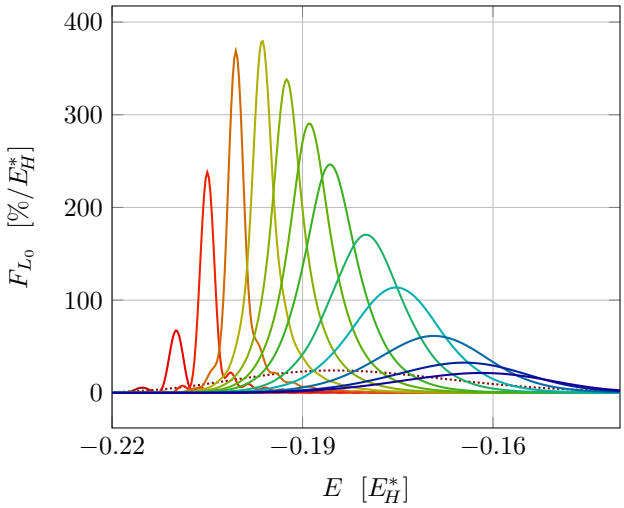

Figure 6. Visualization of the quantum size effect of the ICEC flux densities (Eq. (29)). They are displayed as solid lines for the full range of $\mathscr{L}_L$, where the red curve with peak maximum to the left belongs to $\mathscr{L}_L = 2.77\,a_B^*$ and the blue one to the right to $\mathscr{L}_L = 2.11\,a_B^*$. The overall energy density distribution (dashed line) of Eqs. (7) and (36) is also shown.

that the impulse related contribution exhibits a dispersed root-mean-square width with respect to the initial minimum-uncertainty wavepacket which we attribute to the time passed between the release of the initial wavepacket and the impact on the initially bound electron. Last but not least, we observe that for the extended range of confinement sizes above $\mathscr{L}_L = 2.83\,a_B^*$ (Fig. 3, top left), major contributions to the flux from the ICD subprocess lie partially outside the confidence interval provided by the initial energy distribution. The definition of the electron capture probability Eq. (40) shown as blue dashed line in Fig. 5 with ordinate on the right hand side is therefore of limited use in cases where the flux maximum position differs largely from the energy distribution maximum. As the capture probability partially encrypts the signature of the probing wavepacket, so does to a lesser extent the maximum of released electron flux density. In the overview of Fig. 6 we hence used $F(E)$. In addition, in Fig. 3 (d) we plot the electron flux density and its integral as function of confinement size $\mathscr{L}_L$. One can observe how ICEC becomes negligible outside a certain region of $\mathscr{L}_L$ and corresponding energies E. For $\mathscr{L}_L < 2.11\,a_B^*$ no $|L_1\rangle$ level exists and this corresponds to flux maxima at larger energies $E > -0.16\,E_H^*$ whereas in the inverse case for $\mathscr{L}_L > 2.77\,a_B^*$ at energies $E < -0.21\,E_H^*$ the two ICEC pathways do start to not overlay in energy. In between maximal fluxes are reached for energetically overlapping channels which not only agrees with former results,[29] but reveals further the detailed reason. Note that of all quantities $\langle V_{12}\rangle$ and

$\int F_{L_0}(E)dE$ in Fig. 3 (b) and (d) align most closely indicating that the flux probability follows tightly the Coulomb interaction.

V. CONCLUSION

In this study, we investigated the quantum size effect of inter-Coulombic electron capture (ICEC) within an established linear model of a nanowire, where a free-moving electron is being confined into an embedded quantum dot through long-range energy transfer onto a bound electron in a nearby confinement. We used electron-dynamics computations to analyze the ionization flux density coinciding with a ground state population in the capturing quantum confinement region and were able to identify and distinguish contributions of direct impulse and kinetic-to-correlation energy conversion with secondary inter-Coulombic decay (ICD). While the ICEC related electron flux density has served here to distinguish between the reaction pathways and their respective contributions at different quantum-dot sizes, we intend to investigate energy relations optimizing or restricting ICEC probability density in a following study.[47] The first hint in that direction was already obtained here, as we numerically evaluated the size dependence of single-electron eigenstates for the investigated confinement sizes, expectation values of electron-electron distance and Coulomb interaction energy of correlation-perturbed doubly-bound two-electron states and found that the Coulomb interaction and the integrated flux density follow each other.

ACKNOWLEDGMENTS

The authors would like to express their gratitude for funding by Volkswagen foundation through the Freigeist grant No. 89525, ER was additionally funded by the HZB Summer Student program. FMP acknowledges SECYT-UNC and CONICET (PIP-11220150100327CO) for partial financial support. The authors thank Victoria Noel.

REFERENCES

[1]G. Moore, Understanding Moore's Law: Four Decades of Innovation , 67 (2006).

[2]Computer companies raced to be the first to release a revolutionizing *486* personal computer towards the end of 1989. Based on the Intel 80486 microprocessor, these computers had already

passed the 800-nm node and were to make personal computers *affordable* (with prices between $10,000 and $20,000 at their launch).[71,72].

[3]K. Mistry, C. Allen, C. Auth, B. Beattie, D. Bergstrom, M. Bost, M. Brazier, M. Buehler, A. Cappellani, R. Chau, C. . Choi, G. Ding, K. Fischer, T. Ghani, R. Grover, W. Han, D. Hanken, M. Hattendorf, J. He, J. Hicks, R. Huessner, D. Ingerly, P. Jain, R. James, L. Jong, S. Joshi, C. Kenyon, K. Kuhn, K. Lee, H. Liu, J. Maiz, B. McIntyre, P. Moon, J. Neirynck, S. Pae, C. Parker, D. Parsons, C. Prasad, L. Pipes, M. Prince, P. Ranade, T. Reynolds, J. Sandford, L. Shifren, J. Sebastian, J. Seiple, D. Simon, S. Sivakumar, P. Smith, C. Thomas, T. Troeger, P. Vandervoorn, S. Williams, and K. Zawadzki, in *2007 IEEE International Electron Devices Meeting* (2007) pp. 247–250.

[4]S. Natarajan, M. Agostinelli, S. Akbar, M. Bost, A. Bowonder, V. Chikarmane, S. Chouksey, A. Dasgupta, K. Fischer, Q. Fu, T. Ghani, M. Giles, S. Govindaraju, R. Grover, W. Han, D. G. Hanken, E. Haralson, M. Haran, M. Heckscher, R. Heussner, P. Jain, R. James, R. Jhaveri, I. Jin, H. Kam, E. Karl, C. L. Kenyon, M. Y. Liu, Y. Luo, R. Mehandru, S. Morarka, L. Neiberg, P. Packan, A. Paliwal, C. Parker, P. Patel, R. Patel, C. Pelto, L. C. Pipes, P. Plekhanov, M. Prince, S. Rajamani, J. Sandford, B. Sell, S. Sivakumar, P. Smith, B. Song, K. Tone, T. Tröger, J. Wiedemer, M. Yang, and K. Zhang, in *2014 IEEE International Electron Devices Meeting (IEDM)* (2014) pp. 3.7.1 – 3.7.3.

[5]'Apple introduces iphone xr,' https://www.apple.com/newsroom/2018/09/apple-introduces-iphone-xr/, Apple Inc. Press Release of 2018-09-12 (2018).

[6]'Huawei launches kirin 980, the world's first commercial 7nm soc,' https://consumer.huawei.com/en/press/news/2018/huawei-launches-kirin-980-the-first-commercial-7nm-soc/, Press Release of 2018-08-31 (2018).

[7]E. Vogel, Nature Nanotechnol. **2**, 25 (2007).

[8]S. Datta, Nat. Electron. **1**, 500 (2018).

[9]R. Rossetti, J. L. Ellison, J. M. Gibson, and L. E. Brus, J. Chem. Phys. **80**, 4464 (1984).

[10]A. P. Alivisatos, J. Phys. Chem. **100**, 13226. (1996).

[11]A. P. Alivisatos, Science **271**, 933 (1996).

[12]F. Kuemmeth, K. I. Bolotin, S.-F. Shi, and D. C. Ralph, Nano Lett. **8**, 4506 (2008).

[13]L. Brus, J . Phys. Chem. **90**, 2555 (1986).

[14]N. N. Ledentsov, Semicond. Sci. Technol. **26**, 014001 (2011).

[15]F. Meinardi, H. McDaniel, F. Carulli, A. Colombo, K. A. Velizhanin, N. S. Makarov, R. Simonutti, V. I. Klimov, and S. Brovelli, Nat. Nanotechnol. **10**, 878 (2015).

[16]M. Mansuripur, *Nonlinear Optics*, Nonlinear Optics , OMA2 (2011).

[17]H.-W. Chen, J.-H. Lee, B.-Y. Lin, S. Chen, and S.-T. Wu, Light-Sci. Appl. **7**, 17168 (2018).

[18]Z. Qian, S. Kang, V. Rajaram, C. Cassella, N. E. McGruer, and M. Rinaldi, Nat. Nanotechnol. , 969 (2017).

[19]W. Luo, J. Lai, D. Lu, C. Du, Y. Liu, S. Gong, D. Shi, and C. Guo, J. Phys. B: At. Mol. Opt. Phys. **45**, 035402 (2012).

[20]N. Singh, A. Agarwal, L. K. Bera, T. Y. Liow, R. Yang, S. C. Rustagi, C. H. Tung, R. Kumar, G. Q. Lo, N. Balasubramanian, and D. . Kwong, in *IEEE Electron Device Letters*, Vol. 27 (2006) pp. 383–386.

[21]R. Huang, R. Wang, J. Zhuge, C. Liu, T. Yu, L. Zhang, X. Huang, Y. Ai, J. Zou, Y. Liu, J. Fan, H. Liao, and Y. Wang, in *2011 IEEE Custom Integrated Circuits Conference (CICC)* (2011) pp. 1–8.

[22]D. B. Suyatin, V. Jain, V. A. Nebol'sin, J. Trägårdh, M. E. Messing, J. B. Wagner, O. Persson, R. Timm, A. Mikkelsen, I. Maximov, L. Samuelson, and H. Pettersson, Nature Commun. **5**, 3221 (2014).

[23]R. Leturcq, C. Stampfer, K. Inderbitzin, L. Durrer, C. Hierold, E. Mariani, M. G. Schultz, F. von Oppen, and K. Ensslin, Nat. Phys. **5**, 327 (2009).

[24]J. Salfi, S. Roddaro, D. Ercolani, L. Sorba, I. Savelyev, M. Blumin, H. E. Ruda, and F. Beltram, Semicond. Sci. Technol. **25**, 024007 (2010).

[25]S. Roddaro, A. Pescaglini, D. Ercolani, L. Sorba, and F. Beltram, Nano Lett. **11**, 1695 (2011).

[26]W. G. van der Wiel, S. De Franceschi, J. M. Elzerman, T. Fujisawa, S. Tarucha, and L. P. Kouwenhoven, Rev. Mod. Phys. **75**, 1 (2002).

[27]F. M. Pont, A. Bande, and L. S. Cederbaum, Phys. Rev. B **88**, 241304(**R**) (2013).

[28]A. Bande, F. M. Pont, K. Gokhberg, and L. S. Cederbaum, EPJ Web Conf. **84**, 07002 (2015).

[29]F. M. Pont, A. Bande, and L. S. Cederbaum, J. Phys. **28**, 075301 (2016).

[30]K. Gokhberg and L. S. Cederbaum, J. Phys. B **42**, 231001 (2009).

[31]K. Gokhberg and L. S. Cederbaum, Phys. Rev. A **82**, 052507 (2010).

[32]N. Sisourat, T. Miteva, J. D. Gorfinkiel, K. Gokhberg, and L. S. Cederbaum, Phys. Rev. A **98**, 020701(R) (2018).

[33]L. S. Cederbaum, J. Zobeley, and F. Tarantelli, Phys. Rev. Lett. **79**, 4778 (1997).

[34]U. Hergenhahn, J. Electron Spectrosc. Relat. Phenom. **184**, 78 (2011).

[35]T. Jahnke, J. Phys. B: At. Mol. Opt. Phys. **48**, 082001 (2015).

[36]A. Bande, K. Gokhberg, and L. S. Cederbaum, J. Chem. Phys. **135**, 144112 (2011).

[37]I. Cherkes and N. Moiseyev, Phys. Rev. B **83**, 113303 (2011).

[38]A. Bande, F. M. Pont, P. Dolbundalchok, K. Gokhberg, and L. S. Cederbaum, EPJ Web Conf. **41**, 04031 (2013).

[39]A. C. LaForge, M. Shcherbinin, F. Stienkemeier, R. Richter, R. Moshammer, T. Pfeifer, and M. Mudrich, Nat. Phys. **15**, 247 (2019).

[40]R. A. Wilhelm, E. Gruber, J. Schwestka, R. Kozubek, T. I. Madeira, J. P. Marques, J. Kobus, A. V. Krasheninnikov, M. Schleberger, , and F. Aumayr, Phys. Rev. Lett. **119**, 103401 (2017).

[41]X. Ren, E. Wang, A. D. Skitnevskaya, A. B. Trofimov, K. Gokhberg, and A. Dorn, Nat. Phys. **14**, 1062 (2018).

[42]S. Xu, D. Guo, X. Ma, X. Zhu, W. Feng, S. Yan, D. Zhao, Y. Gao, S. Zhang, X. Ren, Y. Zhao, Z. Xu, A. Dorn, L. S. Cederbaum, and N. V. Kryzhevoi, Angew. Chem. Int. Ed. **57**, 17023 (2018).

[43]V. Averbukh and L. S. Cederbaum, Phys. Rev. Lett. **96**, 4 (2006).

[44]T. Goldzak, L. Gantz, I. Gilary, G. Bahir, and N. Moiseyev, Phys. Rev. B **91**, 165312 (2015).

[45]T. Goldzak, L. Gantz, I. Gilary, G. Bahir, and N. Moiseyev, Phys. Rev. B **93**, 045310 (2016).

[46]A. Haller, D. Peláez, and A. Bande, submitted (2018).

[47]F. M. Pont, A. Molle, E. R. Berikaa, S. Bubeck, and A. Bande, 'Generous geometry-dependence of the inter-coulombic electron capture processes in paired quantum dots,' (2019), in preparation.

[48]H.-D. Meyer, U. Manthe, and L. S. Cederbaum, Chem. Phys. Letters **165**, 73 (1990).

[49]U. Manthe, H.-D. Meyer, and L. S. Cederbaum, J. Chem. Phys. **97**, 3199 (1992).

[50]M. H. Beck, A. Jäckle, G. A. Worth, and H.-D. Meyer, Phys. Rep. **324**, 1 (2000).

[51]H.-D. Meyer, F. Gatti, and G. A. Worth, eds., *Multidimensional Quantum Dynamics* (Wiley-VCH, Weinheim, 2009).

[52]A. Bande, F. M. Pont, K. Gokhberg, and L. S. Cederbaum, EPJ Web Conf. **84**, 07002 (2015).

[53]P. Dolbundalchok, D. Peláez, E. F. Aziz, and A. Bande, J. Comput. Chem. **37**, 2249 (2016).

[54]F. Weber, E. F. Aziz, and A. Bande, J. Comput. Chem. **38**, 2141 (2017).

[55]O. Rosas-Ortiz, N. Fernández-García, and S. Cruz y Cruz, AIP Conference Proceedings **1077**, 31 (2008).

[56]N. Bohr, The London, Edinburgh, and Dublin Philosophical Magazine and Journal of Science **26**, 476 (1913).

[57]D. R. Hartree, Mathematical Proceedings of the Cambridge Philosophical Society **24**, 89–110 (1928).

[58]R. T. Tung, Applied. Phys. Rev. **1**, 011304 (2014).

[59]W. Shockley, Bell Sys. Tech. J. **28**, 435 (1949).

[60]H. Kroemer, in *Proceedings of the IEEE*, Vol. 70 (1982) pp. 13–25.

[61]S. Lee, O. L. Lazarenkova, P. von Allmen, F. Oyafuso, and G. Klimeck, Phys. Rev. B **70**, 125307 (2004).

[62]I. A. Digdaya, G. W. P. Adhyaksa, B. J. Trześniewski, E. C. Garnett, and W. A. Smith, Nat. Commun. **8**, 15968 (2017).

[63]S. A. Dayeh, D. Susac, K. L. Kavanagh, E. T. Yu, and D. Wang, Adv. Funct. Mater. **19**, 2102 (2009).

[64]K. Zhang, Y. Dai, Z. Zhou, S. U. Jan, L. Guo, and J. R. Gong, Nano Energy **41**, 101 (2017).

[65]S. Bednarek, B. Szafran, T. Chwiej, and J. Adamowski, Phys. Rev. B **68**, 045328 (2003).

[66]DLMF, '*NIST Digital Library of Mathematical Functions*,' http://dlmf.nist.gov/, Release 1.0.21 of 2018-12-15 (2018), F. W. J. Olver, A. B. Olde Daalhuis, D. W. Lozier, B. I. Schneider, R. F. Boisvert, C. W. Clark, B. R. Miller and B. V. Saunders (eds.), [Eqs. 7.2.3 and 7.19.3].

[67]R. Kosloff and D. Kosloff, J. Comput. Phys. **63**, 363 (1986).

[68]D. Neuhauser and M. Baer, J. Chem. Phys. **90**, 4351 (1989).

[69]U. V. Riss and H.-D. Meyer, J. Phys. B: At. Mol. Opt. Phys. **26**, 4503 (1993).

[70]U. V. Riss and H.-D. Meyer, J. Chem. Phys. **105**, 1409 (1996).

[71]P. H. Lewis, 'The executive computer; the race to market a 486 machine,' https://www.nytimes.com/1989/10/22/business/the-executive-computer-the-race-to-market-a-486-machine.html, New York Times of 1989-10-22 (1989).

[72]W. Lambrechts, S. Sinha, J. A. Abdallah, and J. Prinsloo, *Extending Moore's Law through Advanced Semiconductor Design and Processing Techniques* (CRC Press / Taylor & Francis Group, Boca Raton (FL), 2019).